scientific reports

Check for updates

OPEN

Comparison of in vitro migration assays evaluating nintedanib's migration inhibitory effects on melanoma cells

Afrodité Németh[1,3], Gréta L. Bányai[1,3], Mátyás Andrészek[1], Nikolett Kitti Dobos[1], Csaba Köllőd[1] & Tamás Garay[1,2]✉

Cell migration plays a central role in tumor progression and metastasis, making it a critical parameter in both cancer biology and therapeutic evaluation. A range of in vitro migration assays are commonly used to assess treatment-induced effects on motility, each with distinct advantages and limitations that must be considered when interpreting results. In this study, we systematically compared four migration assay formats—scratch, zone-exclusion (Z-E), transwell, and single-cell tracking—across five melanoma cell lines treated with the multi-kinase inhibitor nintedanib. Migration inhibition was quantified for each assay, alongside machine learning-based classification to evaluate the discriminative power of assay-derived features in detecting treatment effects. All assays detected inhibitory effects of nintedanib, although response magnitude varied across formats. The transwell assay demonstrated clear inhibition in most lines but was sensitive to morphological changes. Gap closure assay-based migration rankings were influenced by cell size, underscoring the importance of size normalization. Scratch assays exhibited greater variability and potential confounding due to cell damage, while Z-E assays generated more uniform gaps without mechanical disruption. Single-cell tracking enabled high-resolution phenotypic profiling, including cell-specific features such as size and shape, resulting in consistently high classification accuracy. These findings highlight the importance of selecting appropriate assay formats to accurately evaluate migration behavior and the therapeutic efficacy of anti-migratory compounds.

Keywords Melanoma, Cell migration, Single-cell tracking, Scratch assay, Zone-exclusion assay, Transwell assay, Nintedanib

Cell migration is a fundamental cellular process that enables the formation, remodeling, defense, and repair of multicellular organisms[1]. It is essential to key biological processes, including embryogenesis[2,3], neural development[4], immune system function[5] and tissue homeostasis[6,7]. Cell migration relies on actin filaments' dynamic assembly and disassembly, which drives the movement[8]. Generally, cell migration can be described as a 4-step process. Firstly, the cells become polarized, and a protrusion forms at the leading edge, generating new adhesions through integrins. Subsequently, the cell body is pulled forward over these adhesions, while the trailing edge's adhesions are disassembled to facilitate retraction[9–11].

Aberrant regulation of cell migration can contribute to pathological conditions, including autoimmune diseases[12,13] and metastasis formation[14–17]. Cancer cells can migrate from the tumor-stroma interface either individually or collectively[14]. While individual migration is more common, collective invasion, though less frequent, is often more efficient in initiating metastatic spread[18]. As metastasis is the leading cause of cancer-related death[15], cancer cell migration is a heavily researched area[19–23]. Therapies targeting cell migration have become a key focus in efforts to inhibit metastatic progression[24–27]. Several 2D methods exist for analyzing cell migration, with the most common approaches focused on measuring distinct cell behaviors[28].

Wound healing assays are widely used in cancer research to assess cell migration[29–32]. These assays can be performed by manually creating wounds in a confluent cell monolayer[33] or by using inserts to form defined cell-

[1]Faculty of Information Technology andBionics, Pázmány Péter Catholic University, Budapest, Hungary. [2]Divisionof Oncology, Department of Internal Medicine and Oncology, Semmelweis University, Budapest, Hungary. [3]Afrodité Németh and Gréta L. Bányai contributed equally to this work. ✉email: garay.tamas@itk.ppke.hu

free gaps, known as cell exclusion zones[34–36]. While manual scratching is a simple technique that requires no specialized equipment, it often produces uneven wound edges and leaves dead cells or debris that can interfere with analysis. In contrast, cell exclusion zone methods offer more consistent and reproducible outcomes by avoiding these complications[28]. In wound healing and cell exclusion assays, cell migration is monitored over time via microscopy until the gap or scratch is fully closed[32]. A similar technique, the fence assay, involves seeding cells within a circular ring, allowing them to spread outward[37,38]. Less commonly, microbead-based methods are used, where cells are seeded on microbeads and placed into a well; after bead removal, migration is assessed based on cell coverage of the plate[39]. Microfluidic chambers also serve as tools for analyzing cell motility, relying on chemoattractants to direct migration[40,41]. These chambers have the advantage of requiring only small numbers of cells and treatment agents, but frequent media changes are often necessary due to the limited volume[40,41]. Transwell assays are another common approach that employs chemoattractants[42], such as FBS[43] or fibronectin[44] to drive migration. Cells are seeded in the upper chamber and migrate through membrane pores toward the lower chamber, where the chemoattractant is located. After a set incubation period, migrated cells on the lower membrane surface are quantified, making the transwell assay an endpoint measurement[29,42].

However, these assays share several limitations. They often confound cell migration with proliferation, survival, and invasion, combining these distinct processes into a single measured parameter. Additionally, they measure migration in only one direction and do not capture the dynamic properties of cell movement[28,29,45,46]. Furthermore, with microfluidic chambers and transwell inserts, cell size and the ability to deform through pores or channels become important factors influencing the results[47].

On the other hand, tracking individual cells using time-lapse video microscopy provides detailed insights into cell motility dynamics. Moreover, they are free from confounding factors such as proliferation, viability, invasion, and variations in cell size and shape; additionally, treatment agents can spread evenly on the cells[48]. From these tracks, a range of migration-related parameters can be calculated, including: (1) path-based parameters such as total travelled distance, velocity, and average velocity; (2) displacement-based parameters, like mean square displacement (MSD), displacement, and maximum displacement; and (3) directionality-based parameters, such as directionality ratio and turning angle[49].

Understanding cancer cell migration is critical, as metastasis accounts for 90% of cancer-related deaths[15]. Comparing commonly used migration assays is essential to ascertain whether a treatment specifically targets migration, rather than other cellular processes. Inhibiting migration, as the initial step in metastasis, represents a promising therapeutic approach in cancer treatment. However, the accuracy and reliability of assays are vital for determining whether migration is genuinely impeded. To investigate this phenomenon, we focused on melanoma cell lines, given melanoma's highly metastatic nature[50,51]and the pronounced migratory capacity of its cells[52].

While nintedanib (BIBF1120) is known as a potent multi-kinase inhibitor targeting VEGFR, FGFR, and PDGFR pathways[53], its effect on melanoma migration remains largely unexplored. Most studies to date have focused on its anti-fibrotic and anti-angiogenic properties, especially in the context of resistance to targeted therapies. For example, in BRAF mutant melanoma models, nintedanib has been shown to decrease the expression of ECM remodeling markers and delay tumor relapse by suppressing a pro-fibrotic mesenchymal-like state driven by the miR-143/145 cluster[54]. Another study demonstrated that combining nintedanib with immune checkpoint blockade enhanced anti-tumor immunity through cancer-associated fibroblast (CAF) suppression and increased CD8 + T cell infiltration, suggesting a key role in modulating the tumor microenvironment[55]. Additionally, novel delivery systems co-packaging nintedanib with epigenetic inhibitors like ARV-825, have shown promising results in reducing vasculogenic mimicry and clonogenic capacity in vemurafenib-resistant melanoma cells[56]. Moreover, nintedanib treatment of uveal melanoma cells showed reduced metabolic activity and induction of oxidative stress[57].

Nintedanib has been shown to inhibit migration and invasion in other tumor types, including pancreatic cancer[58], glioblastoma[59], lung cancer[60] and mesothelioma[61]. However, studies directly addressing nintedanib's effect on the intrinsic migratory behavior of melanoma cells are limited. Thus, our study not only compares commonly used migration assays, but also provides new insight into the direct effects of nintedanib on melanoma cell motility, a previously uncharacterized but clinically relevant mechanism of action.

Methods

Cell lines and culturing

The A2058 melanoma cell line is available through ATCC, while the WM983B cell line, derived from a metastatic site, is accessible from the Wistar Institute, Philadelphia, PA. Mel Pt-3 pre and Mel Pt-3 post cell lines were derived from the same patient, before and during vemurafenib treatment, respectively. The Mel Pt-4 post cell line was similarly isolated from a patient undergoing vemurafenib therapy at the time of cell collection. The three Mel Pt cell lines were established and kindly provided by Professor Peter Hersey from the Oncology and Immunology Unit, Calvary Mater Newcastle Hospital, and the Kolling Institute, Royal North Shore Hospital, University of Sydney, NSW, Australia[62].

All cell lines were cultured in DMEM (4.5 g/L glucose with L-glutamine and sodium pyruvate, Capricorn-Scientific) supplemented with 10% fetal bovine serum (FBS, EuroClone) and 1% penicillin-streptomycin-amphotericin (Lonza) at 37 °C in a humidified atmosphere of 5% CO_2, unless otherwise indicated.

Cell viability assay

The sensitivity of cell lines to nintedanib (Sigma-Aldrich, St. Louis, MO, USA) was quantitatively assessed using a Sulforhodamine B (SRB) assay, in order to determine the optimal concentration for subsequent migration experiments. Briefly, 3000 cells per well were seeded in 96-well plates and treated with serial dilutions of nintedanib (1–8 μM) in DMEM supplemented with 10% FBS for 72 h. After incubation, cells were fixed with

10% trichloroacetic acid (TCA), and residual TCA was removed by washing. Plates were then air-dried, and cells were stained with SRB dye for 15 min. Excess dye was removed by washing with 1% acetic acid, followed by a second drying step. Protein-bound SRB was solubilized in 10 mM Tris-HCl buffer (pH 8.0), and absorbance was measured at 570 nm to assess cell viability. Based on the SRB viability results (Fig. S1), IC_{50} values were determined by nonlinear regression analysis using GraphPad Prism. Across all melanoma cell lines, the IC_{50} values were above the concentrations applied in migration assays. Accordingly, we selected 1 μM and 2 μM nintedanib for migration assays to minimize cytotoxic effects while enabling detection of migration-specific responses. These concentrations caused minimal viability reduction across the majority of cell lines, allowing for the assessment of motility changes with minimal cofounding from treatment-induced cell death.

Gap closure assays

Two types of gap closure assays were performed: a conventional wound healing assay, in which a scratch was manually introduced into a confluent cell monolayer, and a zone-exclusion (Z-E) assay, utilizing a silicone-based insert (2-well silicone inserts, Ibidi GmbH) to create a defined cell-free gap.

For the scratch assay, 30,000 cells per well were seeded in a 96-well plate to achieve a confluent monolayer. On the following day, scratch regions were created using a sterile pipette tip. The wells were then washed twice with PBS to remove detached cells, and the remaining adherent cells were treated with 1 or 2 μM nintedanib in 150 μL of DMEM supplemented with 10% FBS.

In the insert-based Z-E assay, 2-well silicone inserts were placed in a 24-well plate, and 15,000 cells were seeded into each chamber of the insert in 70–70 μl of DMEM supplemented with 10% FBS. After overnight incubation to promote cell attachment and monolayer formation, the inserts were carefully removed, generating a well-defined insert gap. Following two washes with PBS, the cells were treated with 1 or 2 μM nintedanib in 150 μL of DMEM supplemented with 10% FBS.

Both assay plates were placed on an inverted phase-contrast microscope equipped with an automated motorized stage and a temperature- and CO_2-controlled incubation chamber (37 °C, 5% CO_2). For the scratch assay, four independent experiments were performed on separate plates, with three replicate wells per condition and two non-overlapping images acquired per scratch. For the zone-exclusion assay, four independent experiments were performed with one insert per condition per plate and three fields of view recorded per well. Time-lapse images were captured every 4 h over 72 h.

Image analysis was performed manually using ImageJ software. The cell-free area of each scratch region and insert gap was delineated by hand, and the gap areas were measured at each time point until complete closure was achieved. Fold change in gap area (relative gap area or relative scratch/Z-E area) was calculated as the ratio of the initial gap area to the area at each time point (relative gap area = A_0/A_t), such that values > 1 indicate progressive gap closure. For clarity, this metric is referred to as relative scratch area in the scratch assay and as relative Z-E area in the zone-exclusion assay throughout the manuscript. To enable statistical comparison of closure dynamics, the area under the curve (AUC) was determined from the time-dependent change in gap area curves.

To account for variability in initial gap area and cell size, gap closure relative to cell size was calculated as the difference between the initial and the given timepoint gap area, normalized to the average cell area (Gap closure relative to cell size = $(A_0 - A_t)/A_{cell}$). Average cell area (A_{cell}) was determined exclusively from single-cell videomicroscopy experiments, since cells in gap closure assays were too confluent for reliable size measurement. This value was used as a constant to correct for differences in average cell size between cell lines.

Mean gap closure velocity was calculated as the change in gap area between consecutive time points, divided by the time interval (4 h), and averaged over the observation period (Gap closure velocity = $(A_t - A_{t+1})/\Delta t$).

To quantify the inhibitory effect of nintedanib, Inhibition% was calculated by comparing the AUC of the relative gap area between treated and control conditions:

$$Inhibition\% = 100 * \left(1 - \frac{Mean\ AUC_{control}}{AUC_{\ treated}}\right) \quad (1)$$

Here, the mean operator applies only to the control condition, where the AUC values from all replicates were averaged to provide a robust baseline. Each individual treated sample was then normalized to this averaged control value, ensuring both a consistent reference and sufficient variance representation across conditions.

Statistical analysis was performed using the Kruskal–Wallis test for all comparisons. Statistical significance was considered at $p < 0.05$.

Videomicroscopy for single-cell tracking, cell size, and morphology analyses

For single-cell migration analyses, cells were seeded at a density of 1000 cells per well in 96-well plates. This low-density seeding allowed for multidirectional migration to be observed over an extended period. Following approximately 24 h of incubation to allow for cell attachment, treatment with 1 or 2 μM nintedanib was initiated, while control wells received only DMEM supplemented with 10% FBS. Plates were placed on an inverted phase-contrast microscope equipped with an automated motorized stage and an on-stage incubation chamber maintaining standard incubation conditions (37 °C, 5% CO_2). Images were acquired at 10-min intervals over a total period of 72 h. Three independent experiments were performed on separate plates, with three replicate wells per condition, and two distinct fields of view imaged per well. Prior to cell tracking, time-lapse images were pre-processed using ImageJ. The first frame of each recording was smoothed with a Gaussian blur (σ = 1.4) to reduce noise. Background was then removed via a rolling ball algorithm (12-pixel radius), followed by image inversion and contrast enhancement with a saturation threshold of 0.06. Cell migration trajectories were subsequently analyzed using the semi-automated CellTracker software[63]. The software detects individual cells

in each frame based on intensity and size, and links their centroids across consecutive images to reconstruct trajectories. Two initialization parameters are required: average cell size and average cell velocity (in pixels), for which the software's default values were applied. Tracking continuity was manually verified, then time-resolved x–y coordinates were extracted for each individual cell. The number of trackable cells per field varied depending on the field of view, but we aimed to follow at least ten cells in each image. From these data, several quantitative parameters were calculated: mean velocity, displacement, directionality ratio, and mean squared displacement (MSD).

Average velocity was determined by computing the displacement between each pair of consecutive time points and averaging the resulting instantaneous velocities (i.e., distance divided by time) over the entire trajectory. Displacement was defined as the Euclidean distance between the initial position and the cell's position at a given time point along the trajectory. The directionality ratio was calculated by dividing the net displacement (the straight-line distance between the starting and the end points) by the total path length (the sum of all segmental displacements), providing a measure of path linearity. The ratio approaching 1 indicates straight-line migration, while values closer to 0 reflect more random or circuitous movement. MSD was calculated for each time lag by averaging the squared displacements between all position pairs separated by that time interval. The area under the curve (AUC) for both displacement and MSD over time was computed for each individual cell trajectory using the built-in `trapz()` function in MATLAB.

In parallel, cell size, morphological characteristics, and proliferation were quantified from the same time-lapse image sets using ImageJ. For this analysis, at least ten individual cells were manually outlined in each of six representative fields of view at the 24-h time point. In the case of Mel Pt-4 post cells, an additional measurement was also performed at 4 h to assess early morphological changes, since this cell line reached excessive confluency at later time points in the Transwell assay. Based on these outlines, ImageJ automatically extracted several morphological parameters. Although cell area can vary with cell cycle phase, analyzing multiple cells across different fields of view helped to average out such variability. All experiments were performed under standardized seeding density (1000 cells/well), which minimized potential confluency-related artifacts. The cell size represented the two-dimensional surface covered by each cell. Since morphological parameters were obtained from manually outlined cells, potential bias due to user selection cannot be entirely excluded. To minimize this effect, cells were chosen from multiple independent fields of view, and a relatively large number were analyzed: at least 20 cells from a minimum of five different images per cell line, and up to 44 cells from six images when available. This sampling strategy was intended to reduce subjectivity, as averaging across ≥ 20 cells provides a more robust estimate of morphological feature. Circularity was calculated as 4π multiplied by the area divided by the square of the perimeter, providing a value close to 1 for cells with a circular shape. The aspect ratio (AR) was determined as the ratio of the major to minor axis of the best-fit ellipse, indicating cell elongation. Roundness was computed as 4 times the area divided by π times the square of the major axis, similarly reflecting circular symmetry. Solidity quantified cell boundary regularity as the ratio between the cell area and its convex hull area.

Within the same image sequences, cells were manually counted at the beginning of the recording (0 h) and again at 24 and 48 h. Proliferation rate was calculated by dividing the number of cells at these final time points by the number at baseline, allowing comparison across conditions regardless of incubation duration.

The assess the inhibition effect of nintedanib on cell migration, Inhibition% based on MSD parameter was calculated as:

$$Inhibition\% = 100 * \left(1 - \frac{MSD\ AUC_{treated}}{Mean\ MSD\ AUC_{control}}\right) \quad (2)$$

Statistical analysis was performed using the Kruskal–Wallis test for all comparisons. Statistical significance was considered at $p < 0.05$.

Transwell assay

This migration assay was conducted using hanging cell culture inserts with 8 µm pore size (Sigma-Aldrich). For the transwell assay, inserts were placed into 24-well plates, and 30,000 cells were seeded in the upper chamber in 100 µL of serum-free DMEM. The lower chamber contained 750 µL of DMEM supplemented with 1% FBS to establish a chemoattractant gradient. A low serum concentration was chosen to provide sufficient directional stimulus while minimizing diffusion into the upper chamber. At higher concentrations, rapid equilibration would abolish the gradient and thereby reduce the directional drive for migration. In treatment conditions, both the upper and lower compartments received the same concentration of nintedanib (1 or 2 µM). For A2058, WM983B, Mel Pt-3 pre, and Mel Pt-3 post cell lines, the assay was terminated after 24 h. However, for Mel Pt-4 post cells, the incubation was limited to 4 h due to excessive migration at 24 h, which resulted in near-complete membrane coverage, precluding accurate quantification. Non-migrated cells on the upper surface of the insert membrane were gently removed using cotton swabs. Membranes were then washed with PBS, and cells were fixed with 1 mL of 10% TCA in a 24-well plate. Migrated cells on the lower surface were stained with SRB, and three representative images were captured from randomly selected fields using an inverted microscope equipped with a 10× objective. At least three independent experiments were performed on separate plates, with one insert per condition in each experiment.

Image analysis was performed using ImageJ software. Briefly, images were first split into RGB channels, and the green channel was selected for analysis. As SRB staining produces a pink coloration, the green channel provided high contrast, appearing dark where cells were present, thus allowing for more accurate cell detection. A fixed threshold value of 0.63 was then applied to enhance contrast and facilitate quantification. To reduce

background noise, a minimum filter with a radius of 2–3 pixels was applied, thus particles smaller than that were excluded to eliminate debris and artifacts. Subsequently, particle analysis was conducted to count the number of cells based on the remaining objects. Due to insufficient contrast in WM983B images, cell counts for this line were determined manually. To validate the automated counts, a representative subset of images from each cell line was also analyzed manually. Automated and manual results showed close agreement, with an average deviation of ~5% (range − 18% to + 11%), confirming the reliability of the automated workflow.

To quantify migratory capacity, the migration rate was calculated by dividing the number of cells that migrated through the membrane by the incubation time (migration rate = number of cells/t). This normalization allowed direct comparison between conditions with different incubation durations.

The relative migration was calculated as the ratio of the number of migrated treated cells to the number of migrated control cells (relative migration = treated cell number/control cell number).

To assess the inhibitory effect of nintedanib, the Inhibition% was calculated as follows:

$$Inhibition\% = 100 * \left(1 - \frac{Relative\ migraton_{treated}}{Mean\ relative\ migration_{control}}\right) \quad (3)$$

Statistical analysis was performed using the Kruskal–Wallis test for all comparisons. Statistical significance was considered at $p < 0.05$.

Machine learning evaluation for comparison of migration assays under nintedanib Inhibition

Direct comparison of migration assays is challenging, as they differ in measured parameters, scales, and units. To provide an independent benchmark of assay reliability, we applied a machine learning-based classification approach. The rationale was that assays with higher sensitivity to drug effects should enable more accurate discrimination between control and nintedanib-treated samples. All analyses were conducted using Python. Data storage and processing were performed with the pandas library[64], and machine learning models were implemented using the scikit-learn package[65].

For the scratch and Z-E assays, the input data for the machine learning pipeline consisted of gap areas (μm^2) measured every 4 h until complete gap closure. From these data, the reduction in gap area between two consecutive time points was calculated. To generate additional features, we calculated the mean and standard deviation of the gap area, as well as the kurtosis and skewness of the gap area distribution to capture shape-related characteristics. The time point of complete gap closure was also included. All these features were combined with the original gap area data to form the final dataset.

For single-cell tracking, x–y coordinates over time were transformed such that all trajectories originated from the point (0,0) by subtracting the initial position from each time point. These relative x-y coordinates were used to calculate: (I) path-based parameters: total travelled distance, mean and standard deviation of distances between two consecutive coordinates, average velocity; (II) displacement-based parameters: maximum displacement, MSD; and (III) directionality-based parameters: directionality ratio, the mean and standard deviation of absolute turning angles and their zero-crossing rate, both between consecutive positions and relative to the initial point. In addition, cell profile normalized data were generated by dividing each feature by the corresponding morphological parameters, as cell size, circularity, AR, roundness, and solidity.

With respect to the classification part of the machine learning pipeline, both datasets are handled equivalently. A 10-times five-fold cross-validation approach[66] was employed to train and evaluate the classification accuracy of a random forest model, which contained 500 decision trees as estimators. At the start of the five-fold cross-validation, the data is randomly split into 5 parts. In each fold, one-fifth of the data is reserved for the test step, while the remaining data is used as the training set. After each fold, the classification accuracy of the test set was recorded, and the final accuracy was determined as the mean of all accuracy values obtained across the 10-times 5-fold cross-validation runs. A schematic overview of the machine learning workflow is provided in Fig. S2.

Results

Evaluating the cell lines' migratory capacity with gap closure assays

Two types of gap closure assays were performed: the scratch assay, where scratch areas were manually created with a pipette tip, and the zone-exclusion (Z-E) assay, where Z-E areas were formed using silicone culture inserts. Manual scratching resulted in variable scratch areas (Fig. 1A) and less defined edges (Fig. S3). In contrast, culture inserts produced more defined and consistent Z-E areas (Fig. S4) with wider gaps, although 2 out of 60 inserts generated gap sizes larger than mean ± 2 SD and were therefore excluded from further analysis (Fig. 1B).

The fold change in gap area (relative scratch/Z-E area) varied among the different cell lines. Mel Pt-4 post cells demonstrated the most rapid gap closure, with complete closure observed in both assays within 16 h. The A2058 and Mel Pt-3 pre cells displayed comparable kinetics, reaching complete closure in the scratch assay by 28 h and approaching closure in the Z-E assay by the end of the experiment. Mel Pt-3 post cells achieved complete closure in the scratch assay by 44 h, but did not fully close the Z-E gap within 72 h. WM983B cells showed the slowest migration, with scratch closure occurring by 72 h, while the Z-E area remained only partially closed (Fig. 1C,D). These trends were also reflected in the area under the curve (AUC) values calculated from the gap area reduction curves (Fig. 1E,F). Delayed closure in the Z-E assays is likely attributable to the larger initial gap area compared to the scratch assay.

Evaluating the cell lines' migration dynamics with single-cell tracking

Individual cell tracking enabled the quantitative assessment of multidirectional migration dynamics across cell lines. Four migration parameters were derived from the x-y coordinates: mean velocity, displacement,

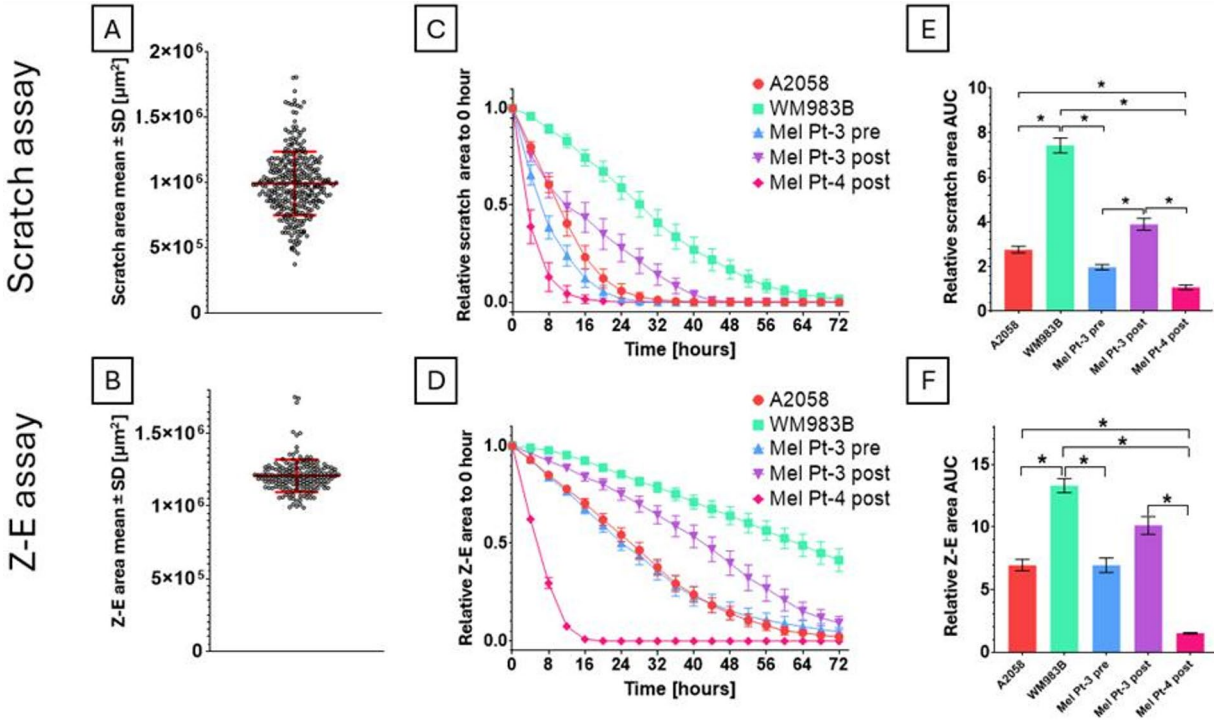

Fig. 1. Evaluating cell lines' migratory capacity with scratch and zone-exclusion (Z-E) assay. (**A**) Manually created scratch areas. Initial scratch area($n = 180$) in the scratch assay; red lines indicate the mean ± SD. (**B**) Z-E areas formed with silicone inserts. Initial Z-E areas ($n = 60$) in the Z-E assay; red lines represent the mean ± SD. (**C**) Relative scratch area over time for each cell line (mean ± SEM, based on $N = 24$ replicates across four independent experiments). (**D**) Relative Z-E area over time for each cell line(mean ± SEM,, based on $N = 12$ replicates across four independent experiments). (**E**) AUC of relative scratch area reduction (mean ± SEM, $N = 24$). (**F**) AUC of relative Z-E area reduction (mean ± SEM, $N = 12$). Replicates with gap sizes outside mean ± 2 SD were excluded as outliers. Statistical analysis was performed using the Kruskal–Wallis test; $p < 0.05$ was considered statistically significant.

directionality ratio, and mean squared displacement (MSD). While mean velocity and directionality were represented as single averaged values per cell line, displacement and MSD were analyzed as time-dependent curves, and their area under the curve was used for quantitative comparisons (Fig. 2).

Among the cell lines, Mel Pt-3 pre cells exhibited the highest mean velocity, followed by Mel Pt-3 post and Mel Pt-4 post cells, which showed comparable speeds. A2058 cells migrated more slowly, while WM983B cells displayed the slowest mean velocity. Regarding displacement, Mel Pt-4 post cells covered the longest distance at 24 h; however, at later time points, A2058 cells surpassed all others, reflecting a more sustained migration behavior over time. Other cell lines showed relatively stable displacement dynamics throughout the observation period. The directionality ratio, reflecting the linearity of the cell movement, was the highest in A2058 cells, indicating that these cells migrated more linearly compared to the other cell lines. This tendency for straighter movement likely contributed to their greater displacement over time. Analysis of the mean squared displacement, which integrates both velocity and directionality, revealed dynamic shifts in migration capability. At 24 h, Mel Pt-4 post cells showed the highest MSD, followed by Mel Pt-3 pre, A2058, Mel Pt-3 post, and WM983B cells. By 48 h, A2058 cells exhibited a higher MSD than both Mel Pt-4 post and Mel Pt-3 pre cells.

Evaluating the cell lines' migratory capacity with the transwell assay

To assess directional chemotactic migration, a transwell assay was performed with a serum gradient, where cells migrated from a serum-free upper chamber toward a lower chamber containing 1% serum. Migration was evaluated after 24 h for all cell lines, except for Mel Pt-4 post, which was analyzed at 4 h. Migration rates were calculated by normalizing the number of migrated cells to incubation time, allowing direct comparison across conditions (Fig. 3).

In the transwell assay, Mel Pt-4 post cells have the highest migratory capacity. Due to extensive membrane coverage, incubation time for this cell line was limited to 4 h, as longer exposure resulted in confluence that hindered reliable quantification. Among the remaining cell lines assessed over 24 h, A2058 cells demonstrated the highest migration rate, followed by Mel Pt-3 pre, Mel Pt-3 post, and WM983B cells, in descending order.

Comparison of gap closure, single-cell tracking, and transwell assays

As gap closure dynamics depend on the initial gap area and cell size (Fig. S5), relative gap closure to 0 h was normalized to cell size (Fig. 4A). This metric increases over time as the gap closes, with faster-closing cell lines

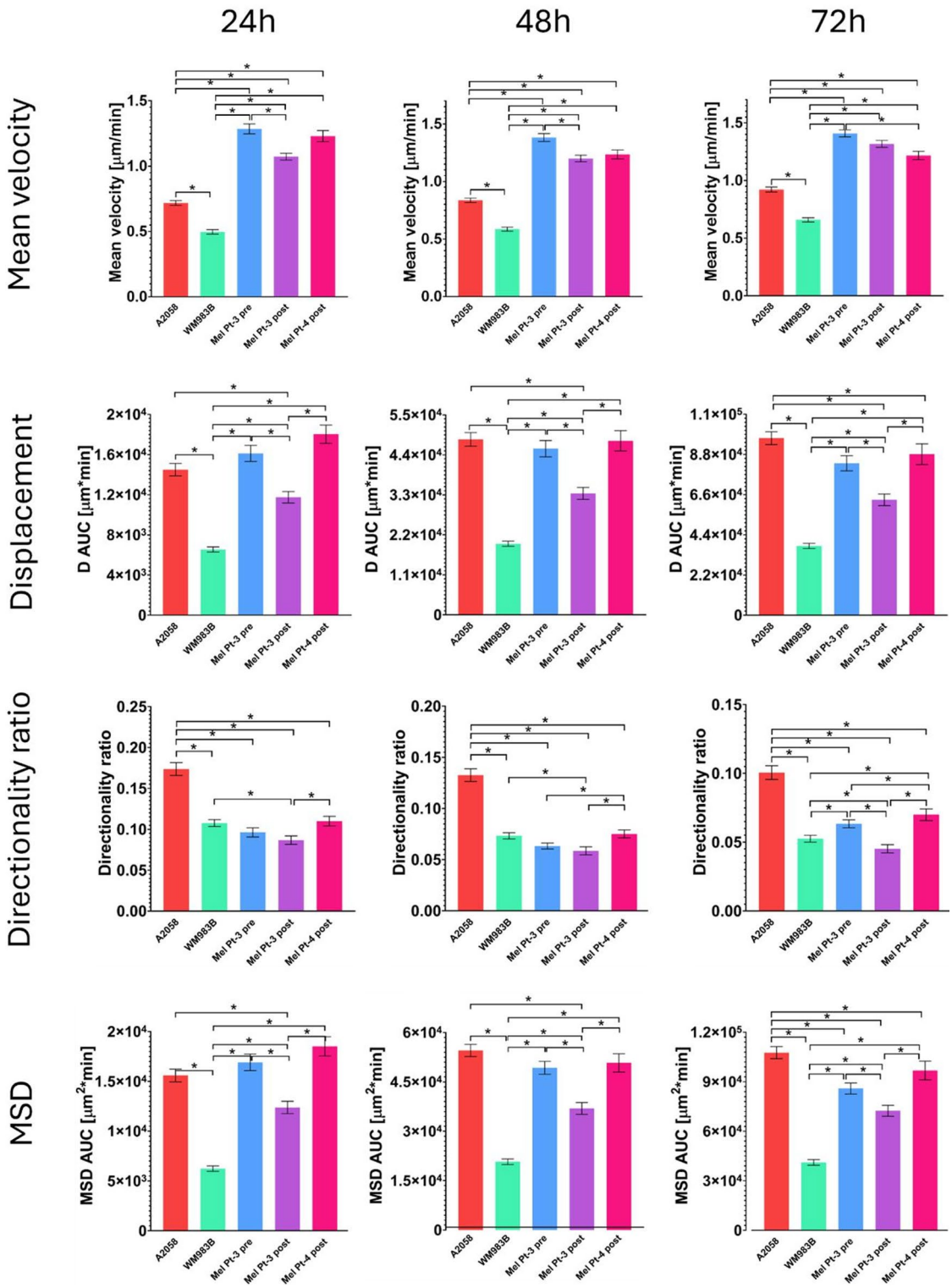

Fig. 2. Evaluating the cell lines' migration dynamics by single-cell tracking. Cell migration was monitored over 72 h, and individual cell trajectories were analyzed using semi-automated tracking in CellTracker. Quantitative parameters – Mean velocity, Displacement (AUC), Directionality ratio, and MSD (AUC) – were calculated. Data represent the mean ± SEM ($N \approx 200–270$ cells per condition; 3 plates × 3 wells × 2 fields, number of trackable cells varied by image). Statistical analysis was performed using the Kruskal–Wallis test; $p < 0.05$ was considered statistically significant.

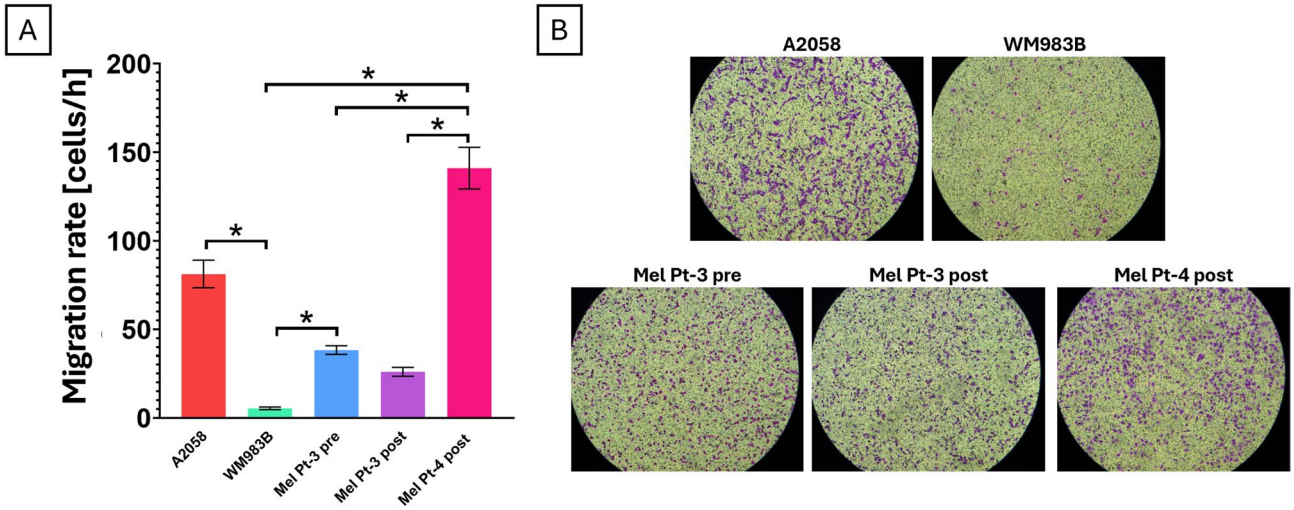

Fig. 3. Evaluating the cell lines' migratory capacity with the transwell assay. (**A**) Cells migrated through an 8 µm pore membrane toward 1% serum for 24 h (4 h for Mel Pt-4 post). Data represent the mean ± SEM of migration rates from at least three independent experiments (at least $N = 9$). Statistical analysis was performed using the Kruskal–Wallis test; $p < 0.05$ was considered statistically significant. (**B**) Representative microscopy images of migrated cells at 24 h (4 h for Mel Pt-4 post).

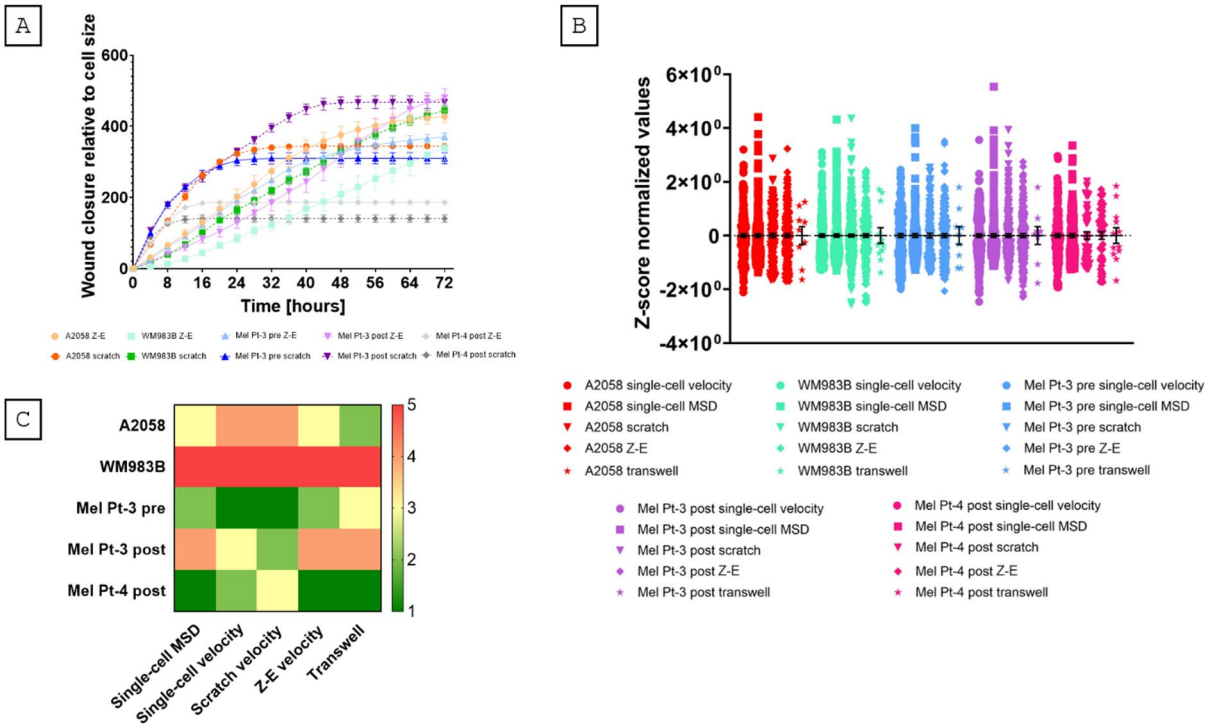

Fig. 4. Comparison of the different migration assays. (**A**) Comparison of scratch and zone-exclusion (Z-E) assays. Gap closure was measured relative to cell size using the mean area obtained from single-cell experiments, to avoid effects of the initial gap area on closure rates. (**B**) Z-score normalized comparison of 24-h migration metrics derived from single-cell MSD and velocity, scratch assay velocity, Z-E assay velocity, and transwell assay results. (**C**) Heat map showing relative cell line rankings across 24-hour migration metrics from single-cell MSD and velocity, scratch assay velocity, Z-E assay velocity, and transwell assay results.

exhibiting steeper, earlier rises in the curve, followed by a plateau as closure nears completion. Closure progression typically slows as the remaining open area diminishes, an overall trend observable across all cell lines. This effect is particularly evident in those that achieved full closure within the 72-h observation period, as the entire closure trajectory, including the deceleration phase, is captured. Across all cell lines, gap closure proceeded more slowly in the Z-E assay compared to the scratch assay, although the overall trends were consistent between methods. Mel Pt-4 post cells exhibited the fastest closure dynamics, with minimal difference between the two assays. A2058 and Mel Pt-3 pre cells followed closely behind, showing similarly efficient closure. In contrast, Mel Pt-3 post and particularly WM983B cells displayed substantially slower progression, with WM983B consistently demonstrating the lowest migratory capacity across both assay types. To assess reproducibility within each assay, Z-score normalization was applied to all quantitative migration metrics (Fig. 4B). In this approach, values are expressed as deviations from the mean of the respective assay, thereby standardizing the distribution and minimizing the influence of absolute scale differences. Importantly, this procedure does not allow direct cross-assay comparison, since the measured parameters differ in units and magnitude; rather, it enables evaluation of variability and consistency within each assay format. The normalized values show relatively modest differences between the various methods and cell lines. Notably, Mel Pt-4 samples appear to exhibit lower variance from the mean across most assays, which may point to more consistent migratory behavior in this cell line.

To enable direct comparison across assay formats, we established relative migration rankings by ordering cell lines according to their 24-h migration metrics (scratch and Z-E closure velocity, transwell counts, single-cell MSD and velocity). This approach allowed us to assess not only absolute values but also the relative consistency of rankings between methods. Migration rankings derived from MSD via single-cell tracking and Z-E velocity yielded similar cell line rankings, closely mirrored by transwell assay, with the only notable difference being the order of Mel Pt-3 pre and A2058 cells (Fig. 4C). Notably, the elevated motility of A2058 observed in the transwell assay aligns with its characteristically linear migration pattern. Mean single-cell velocity and scratch assay velocity displayed a comparable hierarchy, with Mel Pt-4 post and Mel Pt-3 post cells switched in rank. WM983B consistently showed the lowest migratory capacity across all assays. Mel Pt-3 pre and Mel Pt-4 post cells exhibited the highest migratory capacity in 24 h; however, Mel Pt-3 pre cells were less invasive in the transwell assay. Despite appearing slower in the scratch assay, Mel Pt-4 post cells achieved rapid gap closure due to their large size and high migration capacity, though closure time was highly variable and only modestly different from Mel Pt-3 pre and Mel Pt-3 post cells.

Evaluation of nintedanib-induced Inhibition of cell migration using gap closure assays

The sensitivity of each cell line to nintedanib was initially assessed using a total protein-based Sulforhodamine B (SRB) assay (Fig. S1) across a concentration range of 1–8 μM. For migration-specific investigations, where cytotoxicity is not desired, 1 and 2 μM concentrations were selected for further analysis. At these concentrations, relative proliferation rates derived from videomicroscopy confirmed a reduction in proliferation only in A2058 cells at 2 μM, while other cell lines remained largely unaffected (Fig. S6). This approach allowed evaluation of dose-dependent effects of nintedanib on cell migration without substantial impact on cell viability.

To assess the anti-migratory effects of nintedanib, scratch and Z-E assays were repeated under treatment conditions (1 and 2 μM). Relative gap closure was calculated for each time point by normalizing to the initial gap size at $t = 0$ (A_t/A_0), thereby quantifying closure independently of absolute starting dimensions. Area under the curve (AUC) values were then calculated to quantify treatment-induced changes.

Nintedanib consistently reduced cell migration across all cell lines and in both gap closure assays, with measurable effects evident as early as 24 h post-treatment. In both the scratch and Z-E assays, nintedanib treatment led to a dose-dependent delay in gap closure (Fig. 5). In the scratch assay, Mel Pt-3 pre and Mel Pt-4 post cells completed wound closure within 24 h, limiting the detectable impact of 1 μM nintedanib, as no significant inhibition or dose-dependent effect was observed at this early time point (Fig. 5A). Similarly, A2058 cells closed the scratch area by approximately 32 h, and no marked differences was observed between 1 and 2 μM treatments (Fig. 5A). However, in cell lines requiring up to 48 h for closure under control conditions, both nintedanib concentrations significantly reduced migration, with a more pronounced effect observed at 2 μM (Fig. 5A).

In the Z-E assay, Mel Pt-3 pre cells exhibited no significant response to either nintedanib concentration (Fig. 5B). In contrast, the extended closure times allowed for clear detection of inhibition at 2 μM in the remaining four cell lines, indicating a more robust dose-dependent effects on migration in this assay (Fig. 5B).

Evaluation of nintedanib-induced Inhibition of cell migration using single-cell tracking

To investigate the temporal dynamics of nintedanib-induced migration inhibition at the single-cell level, time-lapse tracking was performed over 72 h. Migration parameters, including mean velocity, displacement, directionality ratio, and MSD, were analyzed as previously described. Here, the focus was placed on comparing control and nintedanib-treated cells (1 and 2 μM) over time, to assess dose-dependent effects (Fig. 6). In addition to the AUC-based comparisons, the full temporal profiles of displacement and MSD are provided in Figure S7, illustrating how inhibitory effects evolved dynamically throughout the recorded period.

Nintedanib treatment led to a progressive, dose-dependent reduction in migratory behavior over time. By 24 h, both 1 and 2 μM concentrations significantly decreased mean velocity across most cell lines, with more pronounced inhibition evident at 48 and 72 h. A similar pattern was observed for displacement and MSD, where reduced values became more distinct over time, particularly at the higher dose.

The directionality ratio (DR) showed a more nuanced response. In four of the five cell lines (excluding A2058), nintedanib treatment increased DR by 24 h, indicating straighter migration paths under treatment. However, this effect tended to diminish by 48 and 72 h, with fewer significant differences detected. In contrast, A2058 cells showed a distinct response: although their velocity was less affected compared to other lines, nintedanib

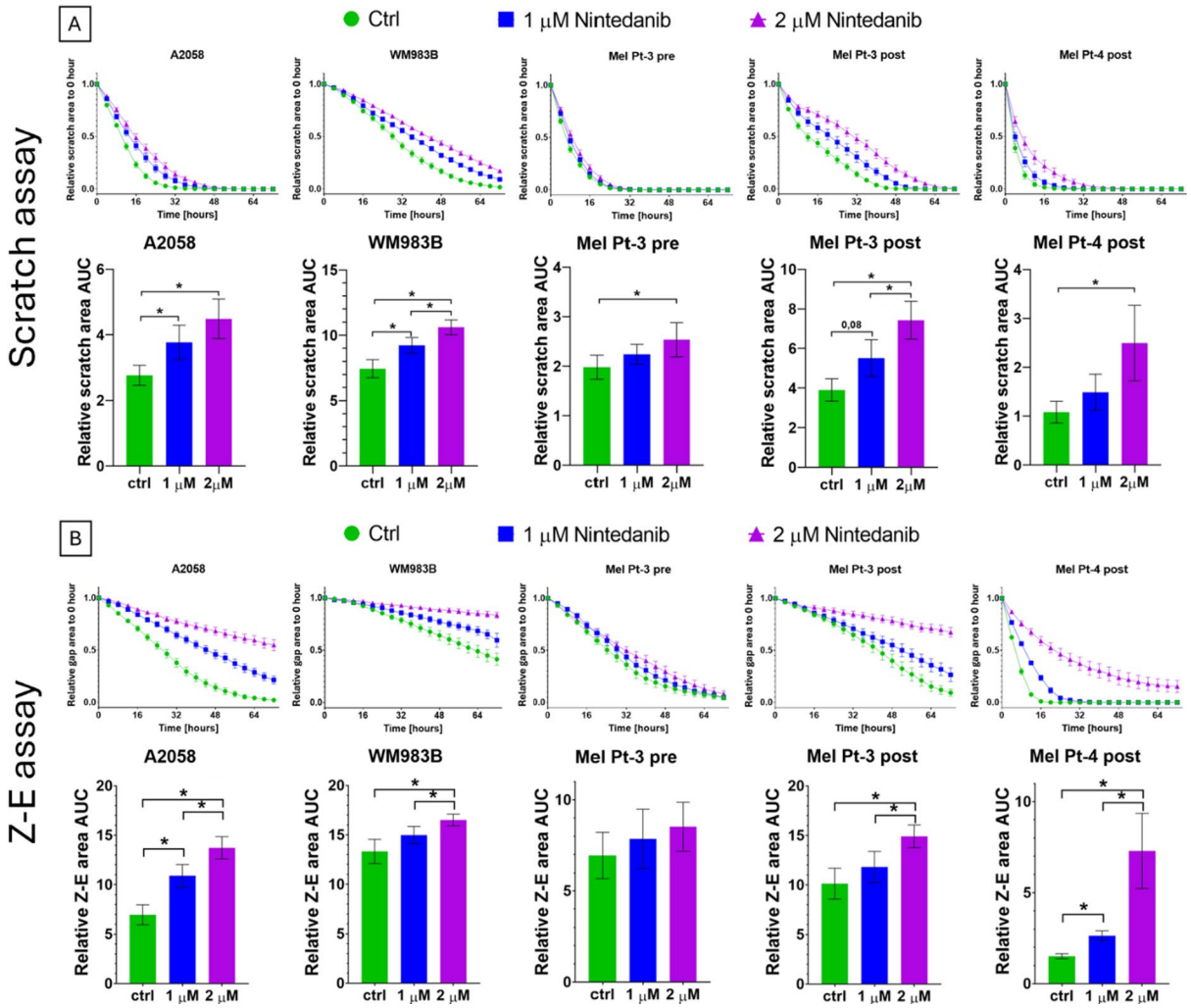

Fig. 5. Evaluating nintedanib effect on cell migration by gap closure assays. Relative scratch (**A**) and Z-E (**B**) areas were normalized to the initial gap size at t = 0 and tracked over time. Corresponding AUC values are shown for each cell line in the presence of 1 or 2 μM nintedanib. Data are shown as mean ± 95% CI, based on $N = 24$ replicates for scratch and $N = 12$ for Z-E across four independent experiment. Replicates falling outside ± 2 SD were excluded as outliers. Statistical analysis was performed using the Kruskal–Wallis test; $p < 0.05$ was considered statistically significant.

markedly reduced their directionality, likely increasing turning behavior and thus leading to a greater reduction in displacement.

Evaluation of nintedanib's effect on cell migration using the transwell assay

The effect of nintedanib on cell migration was further evaluated using the more complex transwell assay, which enables assessment of directional chemotactic migration through a porous membrane in response to a serum gradient. Based on previously established protocols, cells were treated with 1 or 2 μM nintedanib, and their migration toward 1% serum was quantified after incubation (Fig. 7).

Nintedanib treatment resulted in significantly reduced migration in A2058, WM983B, and Mel Pt-3 post cells at both 1 and 2 μM nintedanib concentrations compared to controls. A clear dose-dependent inhibition was observed in A2058 and Mel Pt-3 pre cells, although migration in Mel Pt-3 pre cells was unaffected at 1 μM. Notably, in contrast to findings from other migration assays, Mel Pt-4 post cells displayed an unexpected increase in migration at both nintedanib concentrations, suggesting a distinct, potentially cell line-specific response in the transwell context. This may reflect alterations in cell morphology or deformability under treatment, enabling more efficient transmigration through the porous membrane.

Comparison of migration assays under nintedanib Inhibition and machine learning-based classification of nintedanib response

To systematically compare the sensitivity of different migration assays to nintedanib-induced inhibition, we computed a percentage inhibition value (Inhibition%, Eqs. (1–3)) for all cell lines and assays. This metric

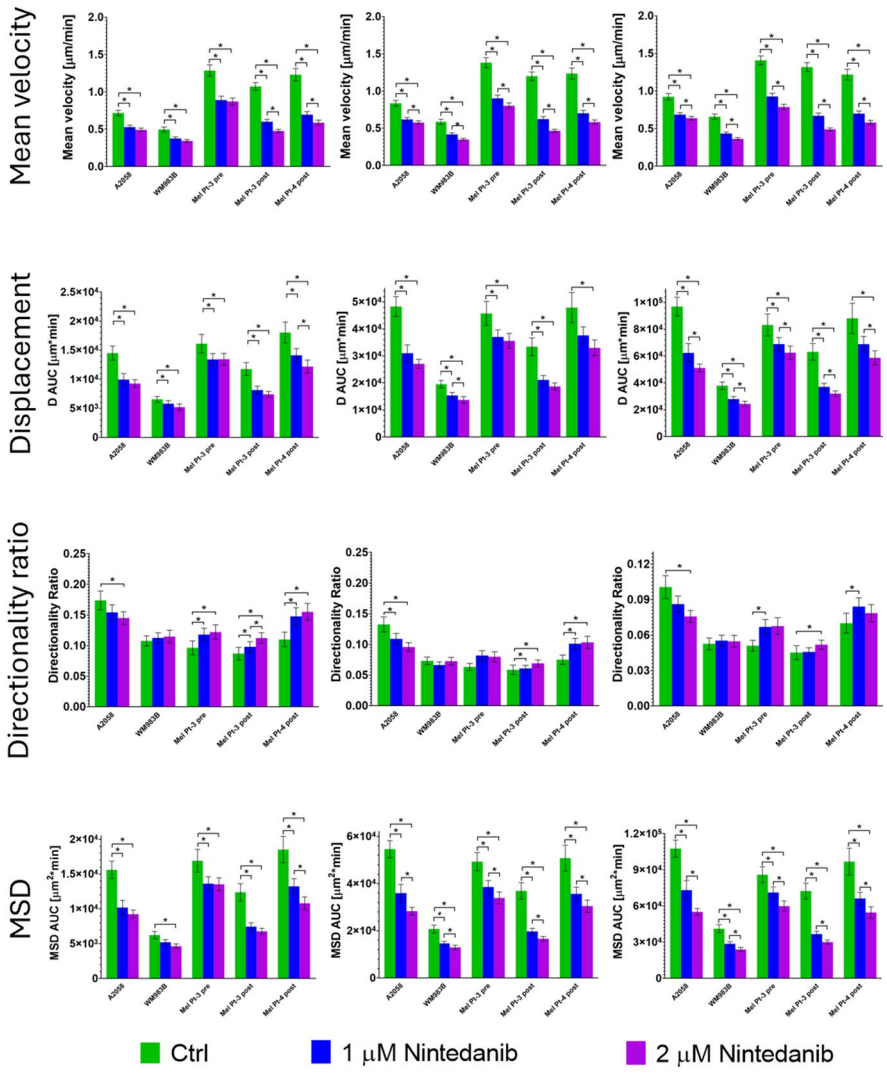

Fig. 6. Evaluating nintedanib's effect on cell migration by single-cell tracking. Cells were treated with 1 or 2 µM nintedanib, and migration was monitored for 72 h. Single-cell trajectories were analyzed using semi-automatic tracking (CellTracker), and migration parameters, mean velocity, displacement, directionality ratio, and MSD, were calculated. Data represent mean ± 95% CI ($N \approx 240–340$ cells per condition; 3 plates × 3 wells × 2 fields, number of trackable cells varied by image). Statistical analysis was performed using the Kruskal–Wallis test; $p < 0.05$ was considered statistically significant.

quantifies the extent to which nintedanib suppresses cell motility relative to untreated controls, allowing cross-assay comparison of drug effects. Higher values correspond to stronger inhibition (Fig. 8A).

In parallel, we applied a machine learning–based classification approach to assess how effectively each assay could distinguish between untreated and nintedanib-treated samples. A machine learning-based random forest model was trained using quantitative features extracted from the scratch assay, the Z-E assay, and the single-cell migration assay. The transwell assay was excluded due to its endpoint nature, which limits the extraction of temporally dynamic features required for classification. The model was built using the top 15 discriminative parameters, selected based on their capacity to separate control samples, and was then tested for its ability to classify all treatment conditions (control, 1 µM, and 2 µM nintedanib) (Fig. 8B).

Across all assays and melanoma cell lines tested, nintedanib consistently exhibited migration-inhibitory effects, with the sole exception observed in Mel Pt-4 post cells in the transwell assay, where an unexpected increase in migration was detected.

At 1 µM nintedanib, single-cell tracking showed significantly higher Inhibition% than the scratch assay for A2058 and Mel Pt-3 post cells. In the Mel Pt-3 post cells, the Z-E assay also showed greater inhibition than single-cell tracking, particularly at 2 µM. In the Mel Pt-4 post cells, the Z-E assay detected a considerably higher inhibition compared to single-cell tracking (Fig. 8A).

Importantly, the feature set derived from the single-cell assay was not limited to standard motility parameters. Unlike collective migration assays, this format allows individual cells to be tracked in isolation, enabling the measurement of cell-intrinsic characteristics such as size and shape. These cell-specific features provide valuable

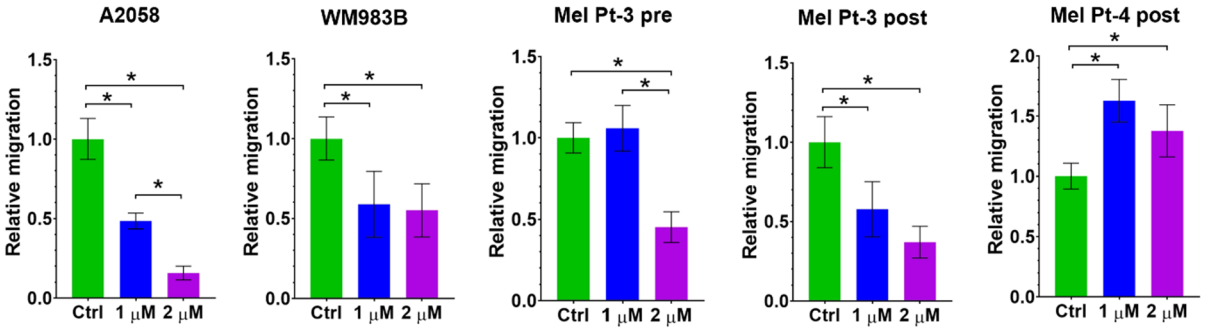

Fig. 7. Evaluating nintedanib's effect on cell migration by transwell assay. Cells were seeded in serum-free medium containing either 1 or 2 μM nintedanib in the upper chamber and allowed to migrate toward a lower chamber containing 1% serum and the corresponding nintedanib concentration. Migration was assessed after 24 h (A2058, WM983B, Mel Pt-3 pre, Mel Pt-3 post) or 4 h (Mel Pt-4 post). Relative migration was calculated as the ratio of migrated treated cells to controls. Data represent mean ± 95% CI of at least three independent experiments (at least $N = 9$). Statistical analysis was performed using the Kruskal–Wallis test; $p < 0.05$ was considered statistically significant.

additional context, as treatments can influence not only migratory behavior but also fundamental cellular properties. Incorporating such features into the classification model markedly enhanced its performance, achieving unambiguous classification accuracy (100%) across all cell lines and treatment conditions (Fig. 8B).

Notably, between the two gap closure assays, significant differences in Inhibition% were only observed in Mel Pt-4 post cells, where the Z-E assay detected greater inhibition than the scratch assay. In A2058 cells, both concentrations of nintedanib led to higher Inhibition% in the transwell assay compared to the scratch assay. Additionally, at 2 μM, the Z-E assay yielded lower Inhibition% than the transwell assay. Similarly, in Mel Pt-3 pre cells, both gap closure assays reported considerably less Inhibition% than the transwell assay (Fig. 8A).

These Inhibition% patterns were reflected in the performance of the machine learning classification. Classification accuracy based on the scratch and Z-E assays was generally more variable and dependent on the cell line. The lowest classification performance was observed for Mel Pt-3 pre cells, where Inhibition% values were also among the lowest across all assays, suggesting that subtle treatment-induced effects result in poor discriminability. Conversely, the Z-E assay in Mel Pt-4 post cells, which showed pronounced and statistically significant inhibition differences compared to control measurements, achieved classification accuracies exceeding 90%. This positive correlation between the magnitude of migration inhibition and classification success was observed consistently across datasets (Fig. 8A).

Finally, the transwell assay demonstrated robust differences in Inhibition%, particularly at 2 μM in A2058, Mel Pt-3 pre, and Mel Pt-3 post cells. Interestingly, and in contrast to all other assays, Mel Pt-4 post cells exhibited a consistent increase in migration under treatment in the transwell assay, suggesting an assay-specific morphological or context-dependent effect (Fig. 8A).

Discussion

Cancer mortality is largely driven by metastatic progression, with secondary tumor formation accounting for the majority of cancer-related deaths. Consequently, in vitro assays that quantify cell migration are essential tools in cancer research and drug development, as they allow systematic evaluation of compounds that may interfere with metastatic spread. However, the choice of assay strongly influences how such effects are detected and interpreted. Understanding the relative strengths and limitations of different migration assays is therefore critical to selecting the most appropriate platform for preclinical studies.

This study systematically compared four widely used in vitro migration assays – scratch wound healing, zone-exclusion (Z-E), transwell, and single-cell tracking – across five melanoma cell lines to evaluate their performance in detecting migration inhibition. Nintedanib, a multi-kinase inhibitor commonly applied as a reference anti-migratory compound, was used to benchmark assay sensitivity. Although nintedanib has gained increasing attention in melanoma therapy in recent years[54–57], its direct impact on melanoma cell motility remains poorly characterized. Our results demonstrate that nintedanib dose-dependently reduced the migratory capacity of melanoma cells in most of the investigated assays, which aligns with findings previously reported in other tumor types[58–61]. At the same time, we observed that the magnitude and interpretation of inhibition varied substantially depending on assay format, underscoring the critical impact of methodological choice when assessing cell motility.

Gap closure assays remain the most common format for collective migration studies, yet our results confirm that their reliability varies considerably. The conventional scratch assay produced higher variability in initial gap sizes and uneven wound edges compared to Z-E assay, reducing their reproducibility. Nevertheless, it appeared to show faster closure dynamics than the Z-E assay, which does not damage the adhered cells. This acceleration is unlikely to solely reflect intrinsic motility, as disruption of the monolayer during scratching can release paracrine factors from damaged cells, stimulating migration and potentially confounding treatment effects[67,68]. In contrast, the Z-E assay generated uniform gaps with minimal perturbation, providing greater standardization across replicates. Moreover, closure occurred more slowly, likely because the absence of damage-associated

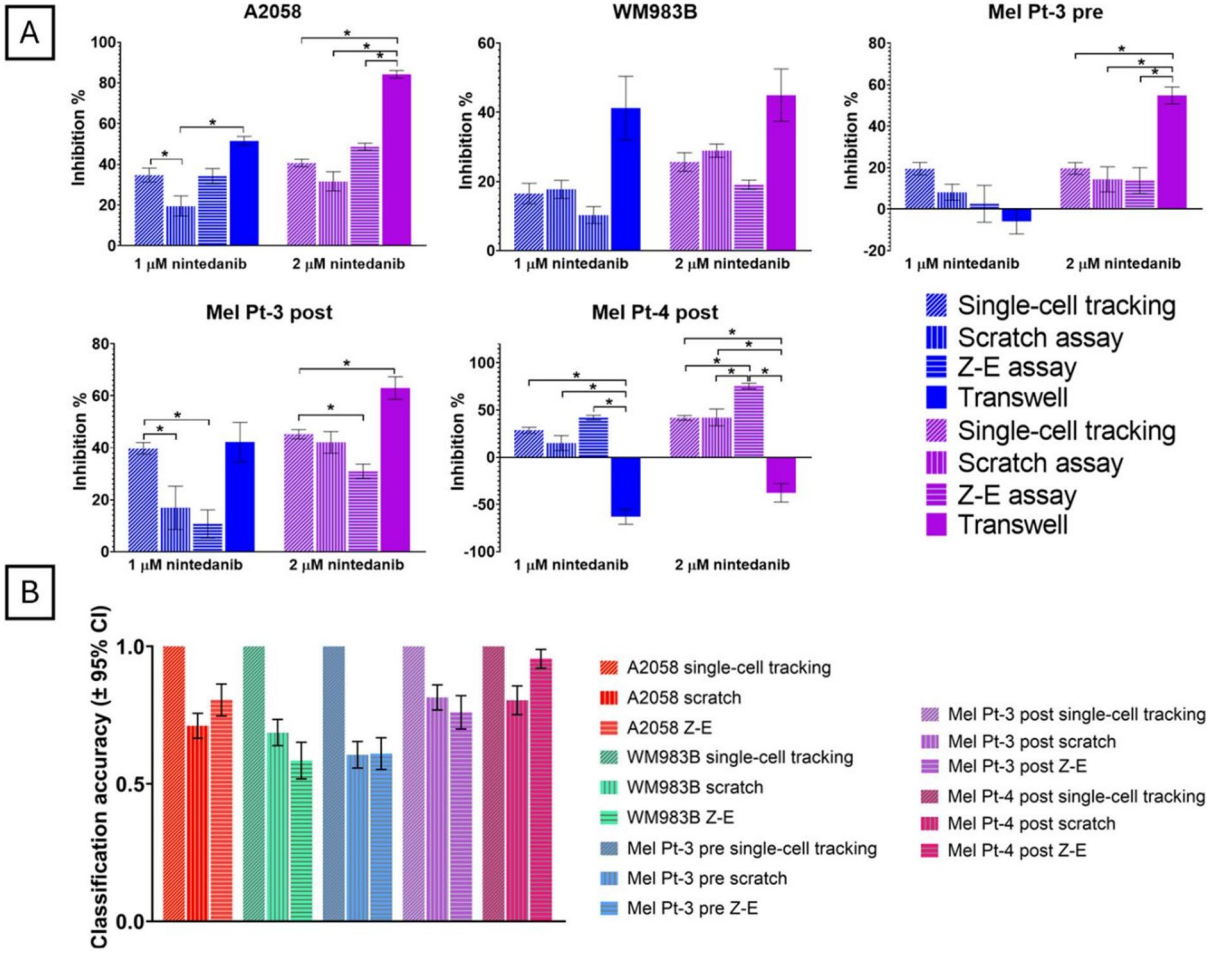

Fig. 8. Comparison of different migration assays under nintedanib treatment. (**A**) To assess the relative sensitivity of each assay, Inhibition% was calculated per cell line. The calculation was based on: 24 h MSD AUC values for single-cell tracking, relative scratch area AUC for scratch assay, relative gap area AUC values for zone-exclusion (Z-E) assay, and relative migration (treated/ control cell number) for transwell assay. Data represent the mean ± SEM of at least three independent experiments. Statistical analysis was performed using the Kruskal–Wallis test; $p < 0.05$ was considered statistically significant. (**B**) Classification accuracy of a machine learning-based random forest model trained to distinguish between control, 1 μM, and 2 μM nintedanib-treated cells across different migration assays (single-cell tracking, scratch, and Z-E assay). Data represent mean classification accuracy per cell line; error bars indicate 95% confidence intervals based on cross-validation.

cues delays migration onset, and the larger, more regular gaps require more time to be invaded. Importantly, closure dynamics were normalized to cell size, confirming that these slower kinetics reflected assay-specific features rather than simply differences in average cell dimensions. A longer incubation period, therefore, appears necessary in Z-E assays to fully capture drug effects. Interestingly, the two gap closure formats also yielded different rankings of cell line motility, with one assay identifying a different line as the fastest compared to the other. These discrepancies emphasize that methodological differences – together with intrinsic factors such as cell size, which strongly influenced closure velocity[69,70] – can substantially alter the relative assessment of migratory capacity. When tested under nintedanib treatment, both assays detected inhibition, but sensitivity varied across cell lines. This pattern was further evident in the machine learning-based classification, where accuracy in detecting treatment effects varied by assay–cell line combination. For instance, Mel Pt-3 pre consistently showed the lowest classification accuracy across both assays, whereas Mel Pt-4 post reached the highest in the Z-E format.

Single-cell tracking offered complementary insights by quantifying spontaneous, multidirectional migration at the level of individual cells. Multiple quantitative parameters can be extracted and classified into three categories: path-based (e.g., velocity), displacement-based (e.g., mean squared displacement (MSD), displacement), and directionality-based (e.g., directionality ratio). Although velocity is the most frequently applied parameter in single-cell migration studies[29,71], our data underscore the importance of integrating multiple metric types. Indeed, rankings differed depending on the chosen parameter: for example, Mel Pt-4 post appeared highest by MSD, whereas velocity analysis ranked Mel Pt-3 pre ahead. These discrepancies illustrate that reliance on a single

Assay	Strengths	Limitations	Context of use
Scratch wound	Simple, rapid setup; consistently showed faster apparent closure than Z-E in both control and nintedanib-treated conditions; inhibition effects appeared relatively consistent across cell lines	High variability in initial gap size and uneven edges; paracrine stimulation from damaged cells may confound drug-specific inhibition	Suitable for preliminary screening and when throughput is important, but interpretation should account for potential overstimulation artifacts
Zone-exclusion (Z-E)	Reproducible and uniform gaps; minimized artifacts from cell damage; in some lines (e.g. Mel Pt-4 post) provided the clearest detection of inhibition	Slower closure dynamics; requires longer incubation; inhibitory effects varied by cell line rather than being uniformly strong	More controlled alternative to scratch; useful when minimizing variability and cell damage is critical
Single-cell tracking	Richest dataset (velocity, MSD, directionality); inhibition by nintedanib was robust across parameters; machine learning achieved 100% accuracy; uniquely allowed quantification of individual cell size and morphology	Labor- and data-intensive; scalability limited; spontaneous migration differs conceptually from collective closure or chemotactic responses	Best suited for precise dissection of drug effects at the single-cell level; the only format that isolates pure migratory behavior, independent of proliferation (gap closure) or deformability (transwell); particularly valuable when cell-intrinsic motility and morphology are central questions
Transwell	Captured chemotaxis and pore traversal (quasi-3D constraint); revealed strongest inhibitory effects overall, except paradoxical increase in Mel Pt-4 post due to reduced cell size (Fig. S6)	Highly sensitive to morphology and cell size; pore passage may mask true inhibitory effects; results less reproducible when image numbers are low	Valuable for invasion- or chemotaxis-focused studies; important to interpret results together with morphological readouts

Table 1. Comparative summary of migration assay performance in this study. Strengths, limitations, and recommended contexts of use are summarized for each assay type based on our experimental results with five melanoma cell lines under nintedanib treatment.

metric, such as velocity, may yield an incomplete or even misleading picture of migratory capacity. In practical terms, cells may display high velocities but still cover limited distances if their trajectories are tortuous, while slower cells can achieve greater net displacement if they move more persistently. Multidimensional profiling is therefore essential for accurately capturing single-cell motility and for detecting subtle, treatment-induced changes. Under nintedanib treatment, these multidimensional readouts became even more informative. Beyond descriptive metrics, single-cell tracking also provided the most powerful readout for classification using machine learning. It achieved 100% accuracy in distinguishing treatment conditions across all cell lines, outperforming both gap closure formats. This superior performance likely reflects its ability to capture not only motility but also intrinsic phenotypic features, including cell size and morphology, which proved critical for detecting drug effects. Notably, single-cell tracking fundamentally differs from collective migration assays in that no external incentive drives movement: cells migrate spontaneously rather than in response to wound closure or chemotactic gradients. As a result, it reflects intrinsic motility patterns that are not directly comparable to repair-driven or chemotactic behaviors, which helps explain discrepancies in rankings across assay types.

The transwell format captured yet another dimension of migration, namely chemotaxis and the ability to deform through pores. Unlike gap closure or single-cell assays, this setup introduces a quasi-3D constraint: cells must actively squeeze through a porous membrane, engaging deformation-based mechanics in addition to motility. While this does not fully recapitulate the complexity of 3D ECM invasion, it provides an intermediate perspective between 2D assays and true 3D models. At baseline, results showed a broadly similar but not identical hierarchy compared to gap closure and single-cell assays: Mel Pt-4 post displayed the highest migration, while WM983B consistently remained the lowest. This underscores that transwell migration reflects distinct aspects of motility, particularly chemotactic responsiveness and invasive potential. Under nintedanib treatment, the transwell assay revealed the strongest inhibitory effects across most cell lines. However, Mel Pt-4 post paradoxically displayed increased migration, in contrast to the other assays. This anomaly likely reflects treatment-induced morphology: whereas nintedanib enlarged most cell lines, Mel Pt-4 post cells instead became smaller (Fig. S6), thereby likely facilitating passage through pores. Nintedanib has previously been shown to induce marked changes in cell morphology, including alterations in size and shape[71–74], supporting this explanation. Combined with the intrinsically high motility of Mel Pt-4 post, derived from a vemurafenib-treated patient, this distinct morphological response likely amplified variability and masked inhibitory effects in the transwell assay. Importantly, we deliberately applied sub-cytotoxic concentrations of nintedanib (1–2 μM) to assess migration independently of viability effects (Supplementary Fig. 4). While this strategy minimized confounding by cell death, it may also have increased stochastic variability, particularly in highly motile lines such as Mel Pt-4 post, where random fluctuations could partially obscure treatment responses. A more detailed exploration of cytoskeletal organization and mechanical adaptation in Mel Pt-4 post cells would likely provide further mechanistic insight, but was beyond the scope of this study.

Taken together, our results emphasize that no single assay captures the full complexity of migration and its pharmacological modulation. Baseline motility and drug-induced inhibition did not always correlate across formats, reflecting that each assay highlights distinct biological processes—such as collective closure, chemotaxis, or spontaneous motility—and therefore emphasizes different dimensions of cellular behavior. These considerations are critical when selecting an appropriate method for evaluating anti-migratory effects. To facilitate assay selection in future studies, we provide a comparative overview of strengths, limitations, and contexts of use based on our experimental findings (Table 1).

Several limitations must be acknowledged. First, only five melanoma cell lines were studied. These were chosen for their robust migratory behavior, which enabled meaningful quantitative comparisons; many carcinoma lines (e.g., breast or colon cancer) migrate poorly under comparable conditions, limiting their suitability for such analyses. While our results may not generalize across all tumor types, the methodological insights are broadly applicable. Second, all assays were performed in 2D environments, which cannot fully recapitulate the spatial

and mechanical constraints of 3D tissues, where migration depends on ECM remodeling, protease activity, and deformation through confined spaces[75–80]. Indeed, several groups have shown that cells migrate more slowly but with greater directional persistence in 3D compared to 2D [75, 69], and that pharmacological inhibition can yield divergent outcomes between the two settings[78,79]. These differences highlight that while our transwell assay introduces a quasi-3D element, true 3D systems capture additional matrix-dependent constraints that may critically influence drug responses. Third, although morphology was quantified from multiple fields and averaged across several cells to reduce variability, potential bias introduced by manual outlining cannot be entirely excluded. Finally, while single-cell tracking proved most informative, its labor intensity limits scalability for high-throughput drug discovery, though recent automation efforts may improve feasibility.

This research was funded by the RRF-2.3.1-21-2022-00004 grant of the National Research, Development and Innovation Office in Hungary.

Data availability

Experimental raw data (e.g.: video microscopy recordings) used and analyzed during the current study are available from the corresponding author on reasonable request.

Received: 15 July 2025; Accepted: 29 October 2025
Published online: 28 November 2025

References

1. Boekhorst, V., Preziosi, L. & Friedl, P. Plasticity of cell migration in vivo and in silico. *Annu. Rev. Cell. Dev. Biol.* **32**, 491–526. https://doi.org/10.1146/annurev-cellbio-111315-125201 (2016).
2. Szabó, A. & Mayor, R. Mechanisms of neural crest migration. *Annu. Rev. Genet.* **52**, 43–63. https://doi.org/10.1146/annurev-genet-120417-031559 (2018). PMID:30476447.
3. Olson, H. M. & Nechiporuk, A. V. Using zebrafish to study collective cell migration in development and disease. *Front. Cell. Dev. Biol.* **6**, 83. https://doi.org/10.3389/fcell.2018.00083 (2018).
4. Cooper, J. A. Cell biology in neuroscience: mechanisms of cell migration in the nervous system. *J. Cell. Biol.* **202** (5), 725–734. https://doi.org/10.1083/jcb.201305021 (2013). PMID:23999166; PMCID:PMC3760606.
5. Luster, A. D., Alon, R. & von Andrian, U. H. Immune cell migration in inflammation: present and future therapeutic targets. *Nat. Immunol.* **6** (12), 1182–1190. https://doi.org/10.1038/ni1275 (2005). PMID:16369557.
6. Krndija, D. et al. Active cell migration is critical for steady-state epithelial turnover in the gut. *Science* **365** (6454), 705–710. https://doi.org/10.1126/science.aau3429 (2019).
7. Dekoninck, S. & Blanpain, C. Stem cell dynamics, migration and plasticity during wound healing. *Nat. Cell. Biol.* **21** (1), 18–24. https://doi.org/10.1038/s41556-018-0237-6 (2019).
8. Schaks, M., Giannone, G. & Rottner, K. Actin dynamics in cell migration. *Essays Biochem.* **63** (5), 483–495. https://doi.org/10.1042/EBC20190015 (2019).
9. Iwasa, J., Marshall, W. F. & Karp, G. *Karp's Cell and Molecular Biology: Concepts and Experiments*, 9th edn (Wiley, 2020).
10. Friedl, P. & Wolf, K. Tumour-cell invasion and migration: diversity and escape mechanisms. *Nat. Rev. Cancer.* **3** (5), 362–374. https://doi.org/10.1038/nrc1075 (2003). PMID:12724734.
11. SenGupta, S., Parent, C. A. & Bear, J. E. The principles of directed cell migration. *Nat. Rev. Mol. Cell. Biol.* **22** (8), 529–547. https://doi.org/10.1038/s41580-021-00366-6 (2021). PMID:33990789; PMCID:PMC8663916.
12. Banerjee, S., Nara, R., Chakraborty, S., Chowdhury, D. & Haldar, S. Integrin regulated autoimmune disorders: Understanding the role of mechanical force in autoimmunity. *Front. Cell. Dev. Biol.* **10**, 852878. https://doi.org/10.3389/fcell.2022.852878 (2022).
13. Liu, J. et al. Dendritic cell migration in inflammation and immunity. *Cell. Mol. Immunol.* **18** (11), 2461–2471. https://doi.org/10.1038/s41423-021-00726-4 (2021).
14. Majidpoor, J. & Mortezaee, K. Steps in metastasis: an updated review. *Med. Oncol.* **38** (1), 14. https://doi.org/10.1007/s12032-020-01447-w (2021).
15. Bergers, G. & Fendt, S. M. The metabolism of cancer cells during metastasis. *Nat. Rev. Cancer.* **21** (3), 162–180. https://doi.org/10.1038/s41568-020-00320-2 (2021). PMID:33462499; PMCID:PMC8733955.
16. Bravo-Cordero, J. J., Hodgson, L. & Condeelis, J. Directed cell invasion and migration during metastasis. *Curr. Opin. Cell. Biol.* **24** (2), 277–283. https://doi.org/10.1016/j.ceb.2011.12.004 (2012). PMID:22209238; PMCID:PMC3320684.
17. Novikov, N. M., Zolotaryova, S. Y., Gautreau, A. M. & Denisov, E. V. Mutational drivers of cancer cell migration and invasion. *Br. J. Cancer.* **124** (1), 102–114. https://doi.org/10.1038/s41416-020-01149-0 (2021). PMID:33204027; PMCID:PMC7784720.
18. Strilic, B. & Offermanns, S. Intravascular survival and extravasation of tumor cells. *Cancer Cell.* **32** (3), 282–293. https://doi.org/10.1016/j.ccell.2017.07.001 (2017).
19. Molnár, E. et al. Long-term Vemurafenib exposure induced alterations of cell phenotypes in melanoma: increased cell migration and its association with EGFR expression. *Int. J. Mol. Sci.* **20** (18), 4484. https://doi.org/10.3390/ijms20184484 (2019).
20. Németh, A. et al. Extracellular vesicles promote migration despite BRAF inhibitor treatment in malignant melanoma cells. *Cell. Commun. Signal.* **22**, 282. https://doi.org/10.1186/s12964-024-01660-4 (2024).
21. Wu, J. S. et al. Plasticity of cancer cell invasion: patterns and mechanisms. *Transl. Oncol.* **14** (1), 100899. https://doi.org/10.1016/j.tranon.2020.100899 (2021).
22. Garay, T. et al. Prenylation inhibition-induced cell death in melanoma: reduced sensitivity in BRAF mutant/PTEN wild-type melanoma cells. *PLoS One.* **10** (2), e0117021. https://doi.org/10.1371/journal.pone.0117021 (2015).
23. Yamamoto, A., Doak, A. E. & Cheung, K. J. Orchestration of collective migration and metastasis by tumor cell clusters. *Annu. Rev. Pathol.* **18**, 231–256. https://doi.org/10.1146/annurev-pathmechdis-031521-023557 (2023).
24. Asano, S. et al. Suppression of cell migration by phospholipase C-related catalytically inactive protein-dependent modulation of PI3K signalling. *Sci. Rep.* **7**, 5408. https://doi.org/10.1038/s41598-017-05908-7 (2017).
25. Nguyen, P. L. et al. Suppression of tumor growth and cell migration by indole-based benzenesulfonamides and their synergistic effects in combination with doxorubicin. *Int. J. Mol. Sci.* **23** (17), 9903. https://doi.org/10.3390/ijms23179903 (2022).
26. Gandalovičová, A. et al. Migrastatics—anti-metastatic and anti-invasion drugs: promises and challenges. *Trends Cancer.* **3** (6), 391–406 (2017).
27. Yang, H., Ganguly, A. & Cabral, F. Inhibition of cell migration and cell division correlates with distinct effects of microtubule inhibiting drugs. *J. Biol. Chem.* **285** (42), 32242–32250. https://doi.org/10.1074/jbc.M110.160820 (2010).
28. Kramer, N. et al. In vitro cell migration and invasion assays. *Mutat. Res. Rev. Mutat. Res.* **752** (1), 10–24. https://doi.org/10.1016/j.mrrev.2012.08.001 (2013).
29. Pijuan, J. et al. In vitro cell migration, invasion, and adhesion assays: from cell imaging to data analysis. *Front. Cell. Dev. Biol.* **7**, 107. https://doi.org/10.3389/fcell.2019.00107 (2019).

30. Liu, Z. et al. Hypoxia-induced up-regulation of VASP promotes invasiveness and metastasis of hepatocellular carcinoma. *Theranostics* **8** (17), 4649–4663. https://doi.org/10.7150/thno.26789 (2018).
31. Vierthaler, M. et al. ADCK2 knockdown affects the migration of melanoma cells via MYL6. *Cancers* **14** (4), 1071. https://doi.org/10.3390/cancers14041071 (2022).
32. Martinotti, S. & Ranzato, E. Scratch wound healing assay. *Methods Mol. Biol.* **2109**, 225–229. https://doi.org/10.1007/7651_2019_259 (2020). PMID:31414347.
33. Liang, C. C., Park, A. Y. & Guan, J. L. In vitro scratch assay: a convenient and inexpensive method for analysis of cell migration in vitro. *Nat. Protoc.* 2(2), 329–333. https://doi.org/10.1038/nprot.2007.30 (2007).
34. Shiode, Y. et al. A novel cell exclusion zone assay with a barrier made from room temperature vulcanizing silicone rubber. *Sci. Rep.* **7**, 17383. https://doi.org/10.1038/s41598-017-17646-6 (2017).
35. Veres-Székely, A. et al. Transient agarose spot (TAS) assay: a new method to investigate cell migration. *Int. J. Mol. Sci.* **23** (4), 2119. https://doi.org/10.3390/ijms23042119 (2022).
36. Das, A., Eggermont, A. & ten Hagen, T. A ring barrier–based migration assay to assess cell migration in vitro. *Nat. Protoc.* **10** (6), 904–915. https://doi.org/10.1038/nprot.2015.056 (2015).
37. Fischer, E. G., Stingl, A. & Kirkpatrick, C. J. Migration assay for endothelial cells in multiwells: application to studies on the effect of opioids. *J. Immunol. Methods*. **128** (2), 235–239. https://doi.org/10.1016/0022-1759(90)90215-h (1990). PMID:2139083.
38. Sagnella, S. M. et al. Human microvascular endothelial cell growth and migration on biomimetic surfactant polymers. *Biomaterials* **25** (7–8), 1249–1259. https://doi.org/10.1016/s0142-9612(03)00634-3 (2004).
39. Rosen, E. M., Meromsky, L., Setter, E., Vinter, D. W. & Goldberg, I. D. Quantitation of cytokine-stimulated migration of endothelium and epithelium by a new assay using microcarrier beads. *Exp. Cell. Res.* **186** (1), 22–31. https://doi.org/10.1016/0014-4827(90)90205-o (1990).
40. Shih, H. C. et al. Microfluidic collective cell migration assay for study of endothelial cell proliferation and migration under combinations of oxygen gradients, tensions, and drug treatments. *Sci. Rep.* **9**, 8234. https://doi.org/10.1038/s41598-019-44594-5 (2019).
41. Wong, B. S. et al. A microfluidic cell-migration assay for the prediction of progression-free survival and recurrence time of patients with glioblastoma. *Nat. Biomed. Eng.* **5** (1), 26–40. https://doi.org/10.1038/s41551-020-00621-9 (2021).
42. Justus, C. R., Marie, M. A., Sanderlin, E. J. & Yang, L. V. Transwell in vitro cell migration and invasion assays. *Methods Mol. Biol.* **2644**, 349–359. https://doi.org/10.1007/978-1-0716-3052-5_22 (2023).
43. Omar Zaki, S. S., Kanesan, L., Leong, M. Y. D. & Vidyadaran, S. The influence of serum-supplemented culture media in a transwell migration assay. *Cell. Biol. Int.* **43** (10), 1201–1204. https://doi.org/10.1002/cbin.11122 (2019).
44. Ou, Y. C. et al. Fibronectin promotes cell growth and migration in human renal cell carcinoma cells. *Int. J. Mol. Sci.* **20** (11), 2792. https://doi.org/10.3390/ijms20112792 (2019).
45. Glenn, H., Messner, J. & Meldrum, D. A simple non-perturbing cell migration assay insensitive to proliferation effects. *Sci. Rep.* **6**, 31694. https://doi.org/10.1038/srep31694 (2016).
46. Gau, J. & Roy, P. Single cell migration assay using human breast cancer MDA-MB-231 cell line. *Bio-protocol* **10** (8), e3586. https://doi.org/10.21769/BioProtoc.3586 (2020).
47. Conboy, J. P., Istúriz Petitjean, I., van der Net, A. & Koenderink, G. H. How cytoskeletal crosstalk makes cells move: bridging cell-free and cell studies. *Biophys. Rev. (Melville)*. **5** (2), 021307. https://doi.org/10.1063/5.0198119 (2024). PMID:38840976; PMCID:PMC11151447.
48. Svensson, C. M., Medyukhina, A., Belyaev, I., Al-Zaben, N. & Figge, M. T. Untangling cell tracks: quantifying cell migration by time lapse image data analysis. *Cytometry A*. **93** (3), 357–370. https://doi.org/10.1002/cyto.a.23249 (2018).
49. Masuzzo, P., Van Troys, M., Ampe, C. & Martens, L. Taking aim at moving targets in computational cell migration. *Trends Cell. Biol.* **26** (2), 88–110. https://doi.org/10.1016/j.tcb.2015.09.003 (2016). PMID:26481052.
50. Pagliuca, C., Di Leo, L. & De Zio, D. New insights into the phenotype switching of melanoma. *Cancers* **14** (24), 6118. https://doi.org/10.3390/cancers14246118 (2022).
51. Turner, N., Ware, O. & Bosenberg, M. Genetics of metastasis: melanoma and other cancers. *Clin. Exp. Metastasis*. **35** (5–6), 379–391. https://doi.org/10.1007/s10585-018-9893-y (2018). PMID:29722002.
52. Bonaventure, J., Domingues, M. J. & Larue, L. Cellular and molecular mechanisms controlling the migration of melanocytes and melanoma cells. *Pigment Cell. Melanoma Res.* **26** (3), 316–325. https://doi.org/10.1111/pcmr.12080 (2013). PMID:23433358.
53. Wind, S. et al. Clinical pharmacokinetics and pharmacodynamics of nintedanib. *Clin. Pharmacokinet.* **58** (9), 1131–1147. https://doi.org/10.1007/s40262-019-00766-0 (2019).
54. Diazzi, S. et al. Blockade of the pro-fibrotic reaction mediated by the miR-143/-145 cluster enhances the responses to targeted therapy in melanoma. *EMBO Mol. Med.* **14** (3), e15295. https://doi.org/10.15252/emmm.202115295 (2022).
55. Kato, R. et al. Nintedanib promotes antitumour immunity and shows antitumour activity in combination with PD-1 Blockade in mice: potential role of cancer-associated fibroblasts. *Br. J. Cancer*. **124** (5), 914–924. https://doi.org/10.1038/s41416-020-01201-z (2021).
56. Fu, Y. et al. Development of dual ARV-825 and nintedanib-loaded pegylated nano-liposomes for synergistic efficacy in vemurafenib-resistant melanoma. *Pharmaceutics* **13** (7), 1005. https://doi.org/10.3390/pharmaceutics13071005 (2021).
57. Pawlik, V. E. et al. Impact of nintedanib and anti-angiogenic agents on uveal melanoma cell behavior. *Investig. Ophthalmol. Vis. Sci.* **65** (2), 30. https://doi.org/10.1167/iovs.65.2.30 (2024).
58. Awasthi, N., Hinz, S., Brekken, R. A., Schwarz, M. A. & Schwarz, R. E. Nintedanib, a triple angiokinase inhibitor, enhances cytotoxic therapy response in pancreatic cancer. *Cancer Lett.* **358** (1), 59–66. https://doi.org/10.1016/j.canlet.2014.12.027 (2015). PMID:25527450; PMCID:PMC4450873.
59. Gadhave, D. et al. Quality by design enabled development & in-vitro assessment of a nanoemulgel formulation for nose-to-brain delivery of nintedanib for glioblastoma multiforme treatment. *Int. J. Pharm.* **676**, 125632. https://doi.org/10.1016/j.ijpharm.2025.125632 (2025).
60. Andreucci, E. et al. Nintedanib-αVβ6 integrin ligand conjugates reduce TGFβ-induced EMT in human non-small cell lung cancer. *Int. J. Mol. Sci.* **24** (2), 1475. https://doi.org/10.3390/ijms24021475 (2023).
61. Laszlo, V. et al. Nintedanib is active in malignant pleural mesothelioma cell models and inhibits angiogenesis and tumor growth in vivo. *Clin. Cancer Res.* **24** (15), 3729–3740. https://doi.org/10.1158/1078-0432.CCR-17-1507 (2018).
62. Lai, F., Jiang, C. C., Farrelly, M. L., Zhang, X. D. & Hersey, P. Evidence for upregulation of Bim and the splicing factor SRp55 in melanoma cells from patients treated with selective BRAF inhibitors. *Melanoma Res.* **22** (3), 244–251. https://doi.org/10.1097/cmr.0b013e328353eff2 (2012). PMID:22516966.
63. Piccinini, F., Kiss, A. & Horvath, P. CellTracker (not only) for dummies. *Bioinformatics* **32** (6), 955–957. https://doi.org/10.1093/bioinformatics/btv686 (2016). PMID:26589273.
64. The pandas development team. pandas-dev/pandas: Pandas . Version latest.Zenodo. https://doi.org/10.5281/zenodo.3509134 (2020).
65. Pedregosa F, Varoquaux G, Gramfort A, Michel V, Thirion B, Grisel O, et al.Scikit-learn: Machine learning in Python. *J. Mach. Learn. Res.* . **12**, 2825–2830 (2011).
66. Browne, M. W. Cross-validation methods. *J. Math. Psychol.* **44** (1), 108–132. https://doi.org/10.1006/jmps.1999.1279 (2000).
67. Radstake, W. E. et al. Comparison of in vitro scratch wound assay experimental procedures. *Biochem. Biophys. Rep.* **33**, 101423. https://doi.org/10.1016/j.bbrep.2023.101423 (2023).

68. Jonkman, J. E. et al. An introduction to the wound healing assay using live-cell microscopy. *Cell. Adh Migr.* **8** (5), 440–451. https://doi.org/10.4161/cam.36224 (2014). PMID:25482647; PMCID:PMC5154238.
69. Kauanova, S., Urazbayev, A. & Vorobjev, I. The frequent sampling of wound scratch assay reveals the opportunity window for quantitative evaluation of cell motility-impeding drugs. *Front. Cell. Dev. Biol.* **9**, 640972. https://doi.org/10.3389/fcell.2021.640972 (2021).
70. Özdaş, S. Knockdown of SET domain, bifurcated 1 suppresses head and neck cancer cell viability and wound-healing ability in vitro. *Turk. J. Biol.* **43** (5), 281–292. https://doi.org/10.3906/biy-1903-71 (2019).
71. Kwak, Y. H., Hong, S. M. & Park, S. S. A single cell tracking system in real-time. *Cell. Immunol.* **265** (1), 44–49. https://doi.org/10.1016/j.cellimm.2010.07.001 (2010).
72. Sheu, C. C. et al. Gene expression changes associated with nintedanib treatment in idiopathic pulmonary fibrosis fibroblasts: a next-generation sequencing and bioinformatics study. *J. Clin. Med.* **8** (3), 308. https://doi.org/10.3390/jcm8030308 (2019).
73. Schelch, K. et al. FGF2 and EGF induce epithelial–mesenchymal transition in malignant pleural mesothelioma cells via a MAP kinase/MMP1 signal. *Carcinogenesis* **39** (4), 534–545. https://doi.org/10.1093/carcin/bgy018 (2018).
74. Tsutsumi, T. et al. Nintedanib ameliorates experimental pulmonary arterial hypertension via Inhibition of endothelial mesenchymal transition and smooth muscle cell proliferation. *Respir Res.* **20**, 124. https://doi.org/10.1186/s12931-019-1084-0 (2019).
75. Doyle, A. D., Petrie, R. J., Kutys, M. L. & Yamada, K. M. Dimensions in cell migration. *Curr. Opin. Cell. Biol.* **25** (5), 642–649. https://doi.org/10.1016/j.ceb.2013.06.004 (2013).
76. Jalilian, E., Linortner, M. & Uhl, A. Impact of image compression on in vitro cell migration analysis. *Computers* **12** (5), 98. https://doi.org/10.3390/computers12050098 (2023).
77. Cortesi, M. et al. Accurate identification of cancer cells in complex pre-clinical models using a deep-learning neural network: a transfection-free approach. *Adv. Biol.* **8** (11), 2470112. https://doi.org/10.1002/adbi.202470112 (2024).
78. Lin, Y., Silverman-Dultz, A., Bailey, M. & Cohen, D. J. SCRATCH: A programmable, open-hardware, benchtop robot that automatically scratches cultured tissues to investigate cell migration, healing, and tissue sculpting. bioRxiv. https://doi.org/10.1101/2024.08.27.609782 (2024). (Update in: Cell Rep Methods. 2024;4(12):100915. doi:10.1016/j.crmeth.2024.100915).
79. Doğru, D. et al. An automated in vitro wound healing microscopy image analysis approach utilizing U-net-based deep learning methodology. *BMC Med. Imaging*. **24**, 158. https://doi.org/10.1186/s12880-024-01332-2 (2024).
80. Cortesi, M., Pasini, A., Tesei, A. & Giordano, E. AIM: A computational tool for the automatic quantification of scratch wound healing assays. *Appl. Sci.* **7** (12), 1237. https://doi.org/10.3390/app7121237 (2017).

Author contributions

A.N. and G.L.B. contributed equally to this work and share first authorship. A.N., G.L.B., and G.T. contributed to the conceptualization and writing of the manuscript. A.N., G.L.B., and M.A. performed the experiments. A.N., G.L.B., and N.K.D. conducted the data analysis. Cs.K. developed and implemented the machine learning methods. All authors reviewed the manuscript.

Declarations

Competing interests

The authors declare no competing interests.

Additional information

Supplementary Information The online version contains supplementary material available at https://doi.org/10.1038/s41598-025-26571-3.

Correspondence and requests for materials should be addressed to T.G.

Reprints and permissions information is available at www.nature.com/reprints.

Publisher's note Springer Nature remains neutral with regard to jurisdictional claims in published maps and institutional affiliations.

Open Access This article is licensed under a Creative Commons Attribution-NonCommercial-NoDerivatives 4.0 International License, which permits any non-commercial use, sharing, distribution and reproduction in any medium or format, as long as you give appropriate credit to the original author(s) and the source, provide a link to the Creative Commons licence, and indicate if you modified the licensed material. You do not have permission under this licence to share adapted material derived from this article or parts of it. The images or other third party material in this article are included in the article's Creative Commons licence, unless indicated otherwise in a credit line to the material. If material is not included in the article's Creative Commons licence and your intended use is not permitted by statutory regulation or exceeds the permitted use, you will need to obtain permission directly from the copyright holder. To view a copy of this licence, visit http://creativecommons.org/licenses/by-nc-nd/4.0/.

© The Author(s) 2025